Closed-form solutions for the production of ions in the collisionless ionization of gases by intense lasers

Britton Chang, Paul R. Bolton, and David N. Fittinghoff
University of California, Lawrence Livermore National Laboratories, P.O. Box 808, Livermore, California 94550
(Received 29 July 1991; revised manuscript received 26 October 1992)

We derive in closed form the solutions to the rate equations for sequential field ionization of gases by a focused laser beam. We obtain the low-intensity and the high-intensity limits of the ion yield for each charge state produced by the laser pulse. Furthermore we derive the scaling laws for the appearance intensity and the saturation intensity of the ion yield. We find that the appearance intensity depends not only on the binding energy of the ionized electron but also on the quantum numbers of the shell from which the electron ionizes. We interpret this dependence on the quantum number to be the species dependence in the appearance intensities discussed by Meyerhofer and co-workers [Phys. Rev. Lett. **63**, 2212 (1989)]. Formulas for five ionization models are presented.

PACS number(s): 32.80.Rm, 32.80.Wr, 42.50.Hz, 32.80.Fb

I. INTRODUCTION

Although the equations for calculating the ion yield in the ionization of collisionless gases by lasers appear to be simple, no one has yet solved them in closed form. The absence of closed-form solutions severely limits our ability: (i) to predict ion yields for new sets of parameters, (ii) to test the atomic models of ionization, and (iii) to improve these models. Their absence also hampers our ability to use the ionization process for practical applications. For example, closed-form solutions enable us to examine appearance and threshold intensities for ion production easily and to detect any significant deviations from the sequential prediction. Since the ionization of gases is essential for collisionless-recombination lasers [1], relativistic propagation of ionization fronts [2], and competes with the production of higher-order harmonics in optical harmonic generation [3,4], our closed form solutions may also be applicable to investigations in these fields of physics.

TABLE I. Scaling laws and formulas for the simple-atom and cycle-averaged simple-atom models.

Quantity	Simple-atom model	Cycle-averaged simple-atom model
Γ	$\gamma\frac{1}{F_k}\exp\left[-\frac{1}{F_k}\right]$	$\gamma\left[\frac{2}{\pi}\right]\left[\frac{1}{F_k}\right]K_0\left[\frac{1}{F_k}\right]^{a}$
γ	$6\omega_0 E_k$	$6\omega_0 E_k$
ϕ	$\gamma\left[\frac{2\tau}{1.76}\right]\left[\frac{1}{F_k}\right]K_1\left[\frac{1}{F_k}\right]^{a}$	$\gamma\left[\frac{2\tau}{1.76}\right]\exp\left[-\frac{1}{F_k}\right]$
N_{k+1}	$\gamma\left[\frac{2\tau}{1.76}\right](\pi\rho V_0)(F_k+F_k^2+F_k^3)\exp\left[-\frac{1}{F_k}\right]$	$\gamma\left[\frac{2\tau}{1.76}\right](2\rho V_0)\left[3F_k^2K_1\left[\frac{1}{F_k}\right]+F_kK_0\left[\frac{1}{F_k}\right]+2\mathrm{Ki}_1\left[\frac{1}{F_k}\right]\right]^{b}$
F_{k+1}^{thres}	$\frac{2}{3}E_k^{3/2}/\ln\left[\frac{\gamma\left[\frac{2\tau}{1.76}\right]\left[\frac{\pi}{2}\right]^{1/2}}{0.01}\right]$	$\frac{2}{3}E_k^{3/2}/\ln\left[\frac{\gamma\frac{2\tau}{1.76}}{0.01}\right]$
F_k^{sat}	$\frac{2}{3}E_k^{3/2}/\ln\left[\frac{\gamma\left[\frac{2\tau}{1.76}\right]\left[\frac{\pi}{2}\right]^{1/2}}{4.605}\right]$	$\frac{2}{3}E_k^{3/2}/\ln\left[\frac{\gamma\frac{2\tau}{1.76}}{4.605}\right]$
F_{k+1}^{ap}	$\frac{2}{3}E_k^{3/2}/\ln\left[\frac{\gamma\left[\frac{2\tau}{1.76}\right](\pi\rho V_0)}{N_{\mathrm{ap}}}\right]$	$\frac{2}{3}E_k^{3/2}/\ln\left[\frac{\gamma\left[\frac{2\tau}{1.76}\right](2\rho V_0)\left[2\left[\frac{\pi}{2}\right]^{1/2}\right]}{N_{\mathrm{ap}}}\right]$

[a] K_1 and K_0 are the modified Bessel functions of the second kind of the order of 1 and 0.
[b] Ki_1 is the repeated integral of K_0 of the order of 1, Sec. 11.2 of Ref. [18].

TABLE II. Scaling laws and formulas for the complex-atom and cycle-averaged complex-atom models.

Quantity	Complex-atom model	Cycle-averaged complex-atom model
Γ	$\gamma\left[\frac{1}{F_k}\right]^{P+1}\exp\left[-\frac{1}{F_k}\right]^{a}$	$\gamma\left[\frac{2}{\pi}\right]\left[-\frac{\partial}{\partial\beta}\right]^{P+1}\frac{1}{\beta}\left[\frac{\beta}{F_k}\right]K_0\left[\frac{\beta}{F_k}\right]$
γ	$\omega_0\tilde{C}_{nl}{}^2G_{lm}\frac{E_k}{2}$ [b]	$\omega_0\tilde{C}_{nl}^2G_{lm}\frac{E_k}{2}$ [b]
ϕ	$\gamma\left[\frac{2\tau}{1.76}\right]\left[-\frac{\partial}{\partial\beta}\right]^{P}\frac{1}{\beta}\left[\frac{\beta}{F_k}\right]K_1\left[\frac{\beta}{F_k}\right]$	$\gamma\left[\frac{2\tau}{1.76}\right]\left[-\frac{\partial}{\partial\beta}\right]^{P}\frac{1}{\beta}\exp\left[-\frac{\beta}{F_k}\right]$
N_{k+1}	$\gamma\left[\frac{2\tau}{1.76}\right](\pi\rho V_0)\left[-\frac{\partial}{\partial\beta}\right]^{P}$ $\times\frac{1}{\beta}\left[\frac{F_k^1}{\beta^1}+\frac{F_k^2}{\beta^2}+\frac{F_k^3}{\beta^3}\right]\exp\left[-\frac{\beta}{F_k}\right]$	$\gamma\left[\frac{2\tau}{1.76}\right](2\rho V_0)\left[-\frac{\partial}{\partial\beta}\right]^{P}\frac{1}{\beta}\left[3\left[\frac{F_k}{\beta}\right]^2K_1\left[\frac{\beta}{K_k}\right]\right.$ $\left.+\frac{F_k}{\beta}K_0\left[\frac{\beta}{F_k}\right]+2\,\mathrm{Ki}_1\left[\frac{\beta}{F_k}\right]\right]$
F_{k+1}^{thres}	$\frac{2}{3}E_k^{3/2}/\ln\left[\frac{\gamma\left[\frac{2\tau}{1.76}\right]\left[\frac{\pi}{2}\right]^{1/2}}{0.01}\right]$	$\frac{2}{3}E_k^{3/2}/\ln\left[\frac{\gamma\frac{2\tau}{1.76}}{0.01}\right]$
F_k^{sat}	$\frac{2}{3}E_k^{3/2}/\ln\left[\frac{\gamma\left[\frac{2\tau}{1.76}\right]\left[\frac{\pi}{2}\right]^{1/2}}{4.605}\right]$	$\frac{2}{3}E_k^{3/2}/\ln\left[\frac{\gamma\frac{2\tau}{1.76}}{4.605}\right]$
F_{k+1}^{ap}	$\frac{2}{3}E_k^{3/2}/\ln\left[\frac{\gamma\left[\frac{2\tau}{1.76}\right](\pi\rho V_0)}{N_{\text{ap}}}\right]$	$\frac{2}{3}E_k^{3/2}/\ln\left[\frac{\gamma\left[\frac{2\tau}{1.76}\right](2\rho V_0)\left[2\left[\frac{\pi}{2}\right]^{1/2}\right]}{N_{\text{ap}}}\right]$

[a] $P=2n-|m|-2$.
[b] Equations (28) and (29) of text.

We have examined five ionization models and have found closed-form solutions for them. These solutions give scaling laws for the appearance intensity as a function of the ionization potential. The scaling laws derived from the static complex-atom model [5,6] and its cycle-averaged variant [5,6] agree with the measured [7–9] appearance intensities better than the scaling laws of the other three examples. Furthermore, the scaling laws for these two models predict the species dependence of the measured appearance intensities for noble gases.

Augst *et al.* [7] have argued intuitively that laser suppression of the Coulomb barrier predicts the species dependence. On the other hand, Gibson, Luk, and Rhodes [8] have argued that barrier suppression could not be the reason for the species dependence because the suppression of the Coulomb barrier yields unrealistically large rates. They concluded that the barrier-suppression model works because of a fortuitous cancellation of errors. We show the species dependence to be a dependence on the quantum numbers of the valence shell from which the electron is removed. This dependence on the quantum numbers arises in the complex-atom model because the rate at which an atom or ion ionizes in this model depends not only on the binding energy of the electron but also on the initial state of the electron.

We also derive saturation intensities from our closed-form solutions. The saturation intensity I_{sat} is where the growth in the ion-yield curve levels off to a $\frac{3}{2}$ power law in intensity. In contrast to experimentally defined appearance intensities, saturation intensities are independent of the ambient gas density. Raising the gas density shifts the ion yield versus intensity curve upwards but does not alter the shape of the curve. If the goal is to use ion yields to measure intensities [10], then the saturation threshold may be a better indicator of intensity than the detection threshold; the density independence of the saturation threshold eliminates an experimental uncertainty.

Tables I–III show our results for five rate laws. The five cases are the following: (i) the static simple atom [11], (ii) the cycle-averaged simple atom, (iii) the complex atom [5,6], (iv) the cycle-averaged complex atom [5,6], and (v) the multiphoton-ionization (MPI) model [12]. We derive only the results for the static simple atom because the reader can easily use the integration technique, provided in Sec. IV, to derive the formulas for cases 2–4. The form of the MPI rate law is different from the other four so the technique is not applicable. However, the MPI rate law is simple enough to permit derivation of the corresponding formulas by direct integration.

II. THE RATE EQUATIONS

We assume that the ambient gas density is low enough that recombination and collisional ionization occur on a

TABLE III. Scaling laws and formulas for the multiphoton-ionization model.

Quantity	Multiphoton-ionization model
Γ	γF_k^{2n} [a]
γ	$6\omega_0 E_k (2n+1)^{2n+1} e^{-(2n+1)}$ [b]
ϕ	$\gamma \left[\frac{\tau}{1.76}\right] B(\frac{1}{2},n) F_k^{2n}$ [c]
N_{k+1}	$\gamma \left[\frac{\tau}{1.76}\right] B(\frac{1}{2},n) \frac{3\pi}{n} \frac{(2n-5)!!}{(2n-4)!!} \rho V_0 F_k^{2n}$
F_{k+1}^{thres}	$\frac{2}{3}E_k^{3/2} \Big/ \left\{ \frac{\gamma \left[\frac{\tau}{1.76}\right] B(\frac{1}{2},n)}{0.01} \right\}^{1/2n}$
F_k^{sat}	$\frac{2}{3}E_k^{3/2} \Big/ \left\{ \frac{\gamma \left[\frac{\tau}{1.76}\right] B(\frac{1}{2},n)}{4.605} \right\}^{1/2n}$
F_{k+1}^{ap}	$\frac{2}{3}E_k^{3/2} \Big/ \left\{ \frac{\gamma \left[\frac{\tau}{1.76}\right] B(\frac{1}{2},n) \frac{3\pi}{n} \frac{(2n-5)!!}{(2n-4)!!} (\rho V_0)}{N_{\text{ap}}} \right\}^{1/2n}$

[a] n is the number of photons required to ionize the atom.
[b] γ was chosen so that the MPI rate law joins smoothly to the simple-atom rate law.
[c] $B(u,v)=\Gamma(u)\Gamma(v)/\Gamma(u+v)$, Eqs. (3.512.2) and (8.384.1) of Ref. [19].

time scale that is greater than the width of the laser pulse and any drift time to a detector. We also assume that ionization occurs sequentially [13]. This model ignores multiple ionization processes in which two or more electrons detach simultaneously (or almost simultaneously) from the atom or from the parent ion. Although some evidence exists for these higher-order processes [14,15], sequential mechanisms describe the bulk of the ion yield [7–9,12,16,17]. The rate equations for sequential ionization under collisionless conditions are

$$\begin{aligned} \frac{dp_0}{dt} &= -\Gamma_0 p_0 , \\ \frac{dp_1}{dt} &= -\Gamma_1 p_1 + \Gamma_0 p_0 , \\ \frac{dp_2}{dt} &= -\Gamma_2 p_2 + \Gamma_1 p_1 , \\ &\cdots \\ \frac{dp_n}{dt} &= \Gamma_{n-1} p_{n-1} . \end{aligned} \tag{1}$$

Here p_k represents the probability that the atom is k times ionized. The rate coefficients Γ_k depend implicitly on both space and time, and are given for example by the dc tunneling formula [11] (which Gibson, Luk, and Rhodes [8] call the static simple atom cases),

$$\Gamma_k = (6\omega_0 E_k) \left[\frac{\frac{2}{3}E_k^{3/2}}{F}\right] \exp\left[-\frac{\frac{2}{3}E_k^{3/2}}{F}\right] . \tag{2}$$

E_k is the twice the ionization potential, the atomic unit of frequency ω_0 is equal to 4.1×10^{16} sec^{-1}, and F represents the space- and time-dependent electric field of the laser. Although we use atomic units in the formulas, we plot the figures in this paper in eV, cm^3, and W/cm^2. Furthermore the numerical examples given in this paper are specifically for argon. We assume that the laser intensity is a focused beam of Gaussian spatial profile with a squared hyperbolic-secant time envelope. The electric field is then

$$F = \frac{F_0}{\left[1+\left[\frac{\lambda z}{\pi w_0^2}\right]^2\right]^{1/2}} \exp\left[-\frac{r^2/w_0^2}{1+\left[\frac{\lambda z}{\pi w_0^2}\right]^2}\right] \times \operatorname{sech}\left[1.76\frac{t}{\tau}\right] . \tag{3}$$

Here F_0 is the peak strength of the electric field, λ is the laser wavelength, w_0 is the $1/e$ radius of the focal spot, and τ is the full width at half maximum of the pulse.

A. Closed-form solutions

The formal solution of Eq. (1) at a fixed point in space is

$$\begin{aligned} p_0(t) &= \exp[-\phi_0(t)] , \\ p_1(t) &= \exp[-\phi_1(t)] \int_{-\infty}^{t} \exp[\phi_1(s)] \Gamma_0(s) p_0(s) ds , \\ p_2(t) &= \exp[-\phi_2(t)] \int_{-\infty}^{t} \exp[\phi_2(s)] \Gamma_1(s) p_1(s) ds , \\ &\cdots \\ p_{n-1}(t) &= \exp[-\phi_{n-1}(t)] \int_{-\infty}^{t} \exp[\phi_{n-1}(s)] \\ &\qquad \times \Gamma_{n-2}(s) p_{n-2}(s) ds , \\ p_n(t) &= \int_{-\infty}^{t} \Gamma_{n-1}(s) p_{n-1}(s) ds , \end{aligned} \tag{4}$$

where ϕ_k is the running integral of Γ_k,

$$\phi_k(t) = \int_{-\infty}^{t} \Gamma_k(t') dt' . \tag{5}$$

It is generally impossible to solve Eq. (4) beyond p_0 in closed form because the higher indexed p_k are multiple integrals of p_0. Figure 1 shows the numerical integration of Eq. (4) for the laser parameters of $I_0=3\times10^{16}$ W/cm^2, $\lambda=616$ nm, $w_0=7$ μm, and $\tau=125$ fs. The time evolution of the ionizing laser pulse, also shown in Fig. 1, reconfirms Lambropoulos's assertion [12] that the rising edge of the intense laser pulse creates the lower charge states.

Figure 1 graphically illustrates the sequential nature of Eq. (1). The low temporal overlap of the probabilities means that the charge states exist sequentially in time, and allows us to simplify Eq. (4). The integrals in Eq. (4) are difficult to solve because they require the probabilities of the lower charge states. For example, solving for p_{k-1}

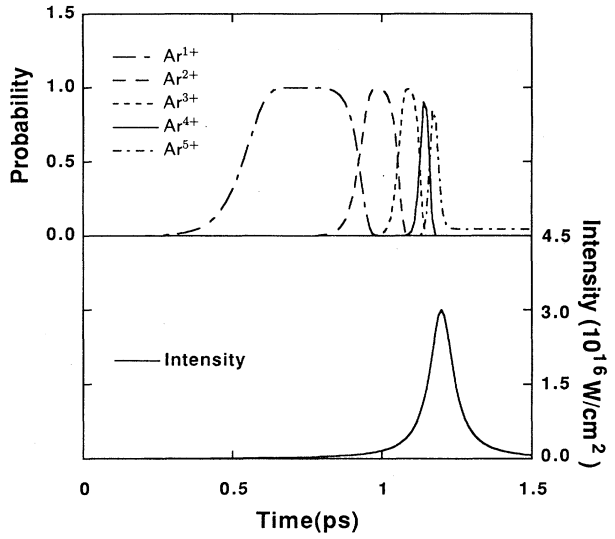

FIG. 1. The time evolution of the ionization state of argon at a fixed point in space with the ionizing laser pulse below. These curves illustrate graphically the sequential ionization process assumed in Eq. (1). They show that the charge states exist in almost nonoverlapping periods of time.

involves the subset of equations for the lower charge states $\{k-2, k-3, \ldots, 0\}$. However, it is not necessary to use the entire subset because the temporal separation implies that the probabilities of the adjacent charge states contain the greatest contribution to p_{k-1}. Furthermore it is sufficient to use only the decaying edge of the lower charge-state probability. Since p_{k-1} can be accurately represented by its decaying edge $\exp(-\phi_{k-1})$ in the integrand of p_k in Eq. (6), the substitution of $\exp(-\phi_{k-1})$ for p_{k-1} in the right-hand side of Eq. (4) yields

$$
\begin{aligned}
&p_0(t)=\exp[-\phi_0(t)] ,\\
&p_1(t)=\exp[-\phi_1(t)]\int_{-\infty}^{t}\exp[\phi_1(s)]\Gamma_0(s)\\
&\qquad\qquad\times\exp[-\phi_0(s)]ds ,\\
&p_2(t)\approx\exp[-\phi_2(t)]\int_{-\infty}^{t}\exp[\phi_2(s)]\Gamma_1(s)\\
&\qquad\qquad\times\exp[-\phi_1(s)]ds ,\\
&\cdots\\
&p_{n-1}(t)\approx\exp[-\phi_{n-1}(t)]\int_{-\infty}^{t}\exp[\phi_{n-1}(s)]\Gamma_{n-2}(s)\\
&\qquad\qquad\times\exp[-\phi_{n-2}(s)]ds ,\\
&p_n(t)\approx\int_{-\infty}^{t}\Gamma_{n-1}(s)\exp[-\phi_{n-1}(s)]ds .
\end{aligned}
\tag{6}
$$

Equation 6 is an exact solution for p_0 and p_1 but is an approximation for the other probabilities.

Equation 6 cannot be evaluated in closed form for an arbitrary laser-pulse envelope. However, for narrow laser pulses, a very good representation for the final probability at the extinction of the pulse is

$$
\begin{aligned}
&p_0(\infty)=\exp(-\phi_0) ,\\
&p_1(\infty)\approx\phi_0\frac{\exp(-\phi_0)-\exp(-\phi_1)}{\phi_1-\phi_0} ,\\
&p_2(\infty)\approx\phi_1\frac{\exp(-\phi_1)-\exp(-\phi_2)}{\phi_2-\phi_1} ,\\
&\cdots\\
&p_{n-1}(\infty)\approx\phi_{n-2}\frac{\exp(-\phi_{n-2})-\exp(-\phi_{n-1})}{\phi_{n-1}-\phi_{n-2}} ,\\
&p_n(\infty)\approx 1-\exp(-\phi_{n-1}) ,
\end{aligned}
\tag{7}
$$

where

$$
\begin{aligned}
\phi_k &\equiv\phi_k(\infty)\\
&=(6\omega_0E_k)\int_{-\infty}^{+\infty}dt\frac{\frac{2}{3}E_k^{3/2}}{F}\exp\left[-\frac{\frac{2}{3}E_k^{3/2}}{F}\right]\\
&=(6\omega_0E_k)\left[\frac{2\tau}{1.76}\right]\frac{2E_k^{3/2}}{3F}K_1\left[\frac{2E_k^{3/2}}{3F}\right]
\end{aligned}
\tag{8}
$$

is the total area under the rate curve. Equation 8 results from the integration of the dc tunneling rate for the hyperbolic secant pulse of Eq. (3) over all time. K_1 in Eq. (8) is the modified Bessel function of the order of 1 [18]. Table I–III give the results for the other rate laws. Figures 2(a) and 2(b) compare Eq. (7) and the results of numerically integrating Eq. (1). We can find no discernible difference between them, and we show in Appendix A that the global error in Eq. (7) is exponentially small.

We can understand intuitively how Eq. (7) follows from Eq. (6) by assuming the rates to be narrow square functions of time. We use τ in Eq. (8) as the widths of the effective square functions, and we use the factors multiplying τ as the heights of the effective square functions. We may also interpret the height of the effective square function H_k as the averaged rate for ionizing charge state k by a square laser pulse of width τ. The substitution $H_k\tau$ for ϕ_k in Eq. (7) would be the result of the substitution and the integration of these square functions in Eq. (6). In Appendix B we prove that the value of every p_k in Eq. (7) is between zero and one. Thus we may still interpret p_k in Eq. (7) as the probability for the charge state k to be present at a given laser intensity.

Equation (7), being the solution to the rate equations of Eq. (1), is a critical formula for two reasons. First, it reduces the time for calculation of the ion yield. The rate equations are stiff differential equations because the rate coefficients differ by many orders of magnitude at each time and because the rate coefficients are very rapidly varying implicit functions of time (according to the laser-pulse envelope); therefore, the numerical integration of Eq. (1) requires small time steps, and is the most time consuming part of the calculation for an ion yield. Second, we can deduce the threshold intensity I_{thres}.

For a given point in space, Eq. (7) gives the final ion balance as a function of intensity. It describes how the population of charge state k (p_1, for example, in Fig. 2) increases and diminishes with intensity. The intensities

marking the onset and extinction of p_1 bear heavily on the shape of the ion-yield curve for the singly ionized atom because we obtain the yield by integrating p_1 of Eq. (7) over all space. Let us call the intensity corresponding to the onset of p_1 the threshold intensity, and the intensity corresponding to the extinction of p_1 the saturation intensity. We will justify this nomenclature below.

B. Threshold and saturation intensities

To determine the threshold and saturation intensities of p_{k+1} in Eq. (7), we need to know the behavior of ϕ_k with respect to the field strength. Figure 3 shows that ϕ_0, for example, increases monotonically with increasing field strength in the manner of a "smoothed" Heaviside step function. For small field strengths, both ϕ_k and ϕ_{k+1} are small [see Fig. 3 or use the asymptotic limit of the Bessel function in Eq. (8) to determine more precisely that they are both of order $\exp(-2E^{3/2}/3F)$]. Therefore p_{k+1} is approximately equal to ϕ_k because the ratio $[\exp(-\phi_k)-\exp(-\phi_{k+1})]/[\phi_{k+1}-\phi_k]$ is close to one,

$$p_{k+1}=\phi_k[1+\tfrac{1}{2}(\phi_k+\phi_{k+1})+\cdots]\geq\phi_k$$
$$=(6\omega_0E_k)\left[\frac{2\tau}{1.76}\right]\frac{2E_k^{3/2}}{3F}\left[\frac{\pi}{2}\frac{3F}{2E_k^{3/2}}\right]^{1/2}$$
$$\times\exp\left[-\frac{2E_k^{3/2}}{3F}\right], \tag{9}$$

where we substitute the asymptotic limit of K_1 for ϕ_k in Eq. (9). The exponential in Eq. (9) gives the rising edge of p_{k+1}, and it shows that p_{k+1} rises steeply from small F. According to Eq. (9), p_{k+1} is identically zero only for F equal to zero; however, p_{k+1} decreases exponentially for small F. We define the threshold field strength to be the value where p_{k+1} is equal to 1%. Solving Eq. (9) for the threshold field strength gives

$$F_{k+1}^{\text{thres}}=\frac{\frac{2}{3}E_k^{3/2}}{\ln\left[\dfrac{(6\omega_0E_k)(2\tau/1.76)\sqrt{\pi/2}}{0.01}\right]}. \tag{10}$$

If p_{k+1} had been one-tenth of 1%, then 0.001 would replace the 0.01 in the denominator of the logarithm's argument in Eq. (10). The threshold field strength is rela-

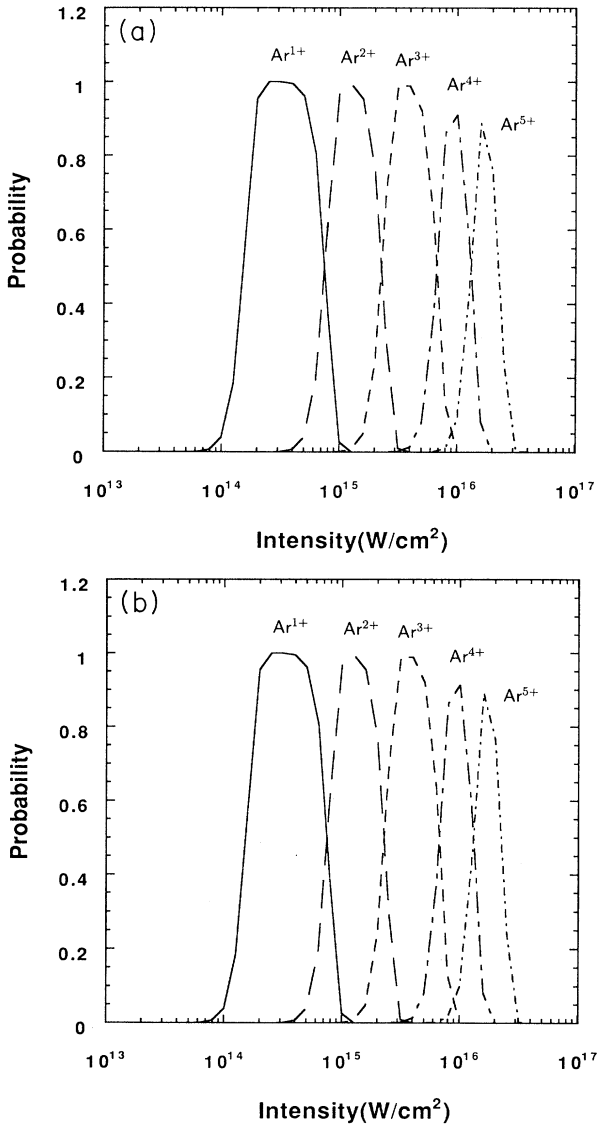

FIG. 2. (a) The numerically calculated ion balance of charge states Ar^{1+}, Ar^{2+}, Ar^{3+}, Ar^{4+}, and Ar^{5+} [final probability of Eq. (4)] is plotted as a function of intensity. (b) The closed-form solution [Eqs. (7) and (8)] to Eq. (1) giving the ion balance of charge states Ar^{1+}, Ar^{2+}, Ar^{3+}, Ar^{4+}, and Ar^{5+}. It agrees almost perfectly with the numerically calculated results of Fig. 2(a).

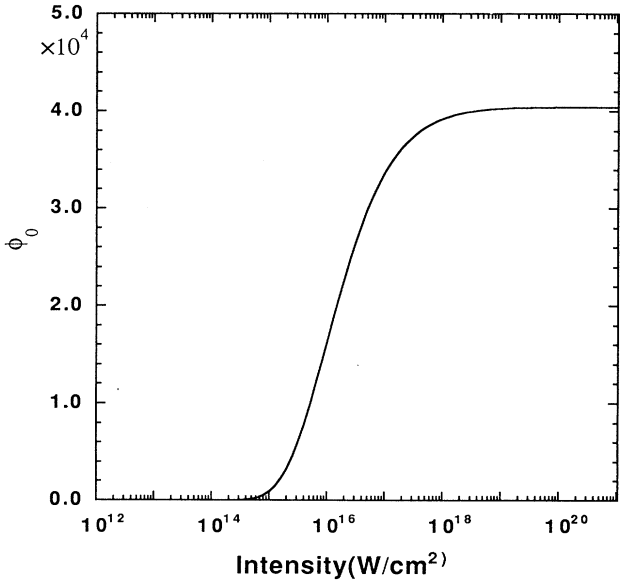

FIG. 3. A plot of ϕ_0, the total area under the rate curve, as a function of intensity. ϕ_k can be thought of as the degree of ionization of charge state k, and it increases monotonically with increasing intensity.

tively insensitive to p_{k+1} (by a factor of a few) because the defining p_{k+1} value is weakened by the logarithm function of Eq. (10), and is also outweighed by the numerator of the logarithm function, which is of order of 10^4. Table IV lists the threshold intensities calculated from Eq. (10) for $k=0,\ldots,4$. A comparison of the threshold intensities in Table IV and Fig. 2 demonstrates the accuracy of Eq. (10).

The threshold field strength defined in the above manner is different from the experimental appearance strength. The threshold field strength is where the ionization probability turns on, but the appearance field strength is defined pragmatically to be the lowest field strength at which an experimenter detects a few ions. Clearly the number of ions detected depends on the ambient gas density and the detection efficiency, so it follows that the appearance field strength does also. The threshold intensity is independent of the ambient gas density because we define it in terms of the ionization probability of a single atom or ion.

Similarly, we define the saturation field strength of p_{k+1} as the field strength where p_{k+1} decreases to the value of .01. As shown in Figs. 2(a) and 2(b), the saturation intensity is greater than the threshold intensity. In this intensity regime, ϕ_k and ϕ_{k+1} are both large. However, ϕ_k is larger than ϕ_{k+1}, so $\exp(-\phi_{k+1})$ dominates $\exp(-\phi_k)$. For high field strengths, p_k is approximately equal to $\exp(-\phi_k)$ because

$$p_{k+1}=\frac{1}{\frac{\phi_{k+1}}{\phi_k}-1}[\exp(-\phi_k)-\exp(-\phi_{k+1})]$$
$$\approx\frac{1}{0-1}[-\exp(-\phi_{k+1})]\ . \tag{11}$$

In this intensity regime, it is also valid to use the asymptotic form of ϕ_{k+1} in Eq. (11). Therefore the saturation field strength is

$$F_{k+1}^{\rm sat}=\frac{\frac{2}{3}E_{k+1}^{3/2}}{\ln\left[\frac{(6\omega_0 E_{k+1})(2\tau/1.76)\sqrt{\pi/2}}{4.605}\right]}\ . \tag{12}$$

The value $4.605=-\ln(0.01)$ in Eq. (12) arises from setting p_{k+1} equal to 0.01 in Eq. (11). An inspection of Table IV and Figs. 2(a) and 2(b) shows that Eq. (12) does not predict the saturation field strength as accurately as Eq. (10) predicts the threshold field strength. This loss of accuracy in predicting the saturation field strength occurs because both ϕ_k and ϕ_{k+1} must be very large for the approximation of Eq. (11) to be valid, but ϕ_k and ϕ_{k+1} are only of the order of a few. Like the threshold field strength, the saturation field strength is independent of the gas density because we define it in terms of probabilities and not in terms of integrated ion counts.

Equations (9) and (11) have simple interpretations for the probability distribution functions shown in Fig. 2(b). The rising edge of p_{k+1} is ϕ_k, and its decaying edge is $\exp(-\phi_{k+1})$. Furthermore, since ϕ_k is the total area under the Γ_k rate curve, ϕ_k represents the degree of ionization of charge state k. Until the laser intensity rises enough to ionize charge state $k+1$, the probability of the ions being in charge state $k+1$ increases with increasing laser intensity. Once the laser intensity rises enough to ionize charge state $k+1$, the probability of the ions being in charge state $k+1$ decays like $\exp(-\phi_{k+1})$.

TABLE IV. Argon threshold and saturation intensities for the simple-atom model calculated using Eqs. (10) and (12). The parameters used are $\omega_0=4.1\times10^{16}$ sec^{-1}, $\tau=1.25\times10^{-13}$ sec, and the E_k's are twice the ionization potentials of argon in atomic units.

Charge state	$I_{\rm thres}$ (W/cm^2)	$I_{\rm sat}$ (W/cm^2)
+1	1.00 (14)	1.32 (15)
+2	5.02 (14)	3.96 (15)
+3	1.56 (15)	1.14 (16)
+4	4.59 (15)	2.19 (16)
+5	8.93 (15)	3.76 (16)

III. ION-YIELD CURVES

To determine the ion yield, we need to integrate Eq. (7) over all space; integrating over isointensity shells greatly simplifies the integration. In mathematical terms, we perform the volume integral by changing the integration variable from volume to intensity. We can enhance our physical understanding (i) of how the change of variable simplifies the spatial integration, and (ii) of the spatial inhomogeneity of the ionization in the focal region of the laser. Figure 4 shows the spatial distributions for Ar^{2+} and Ar^{4+} produced at the focus of the Gaussian beam with a peak intensity of 10^{17} W/cm^2. The ions fall within borders defined by the threshold and saturation isointensity contours. The laser pulse creates the higher charge states close to the focus where the electric field is the

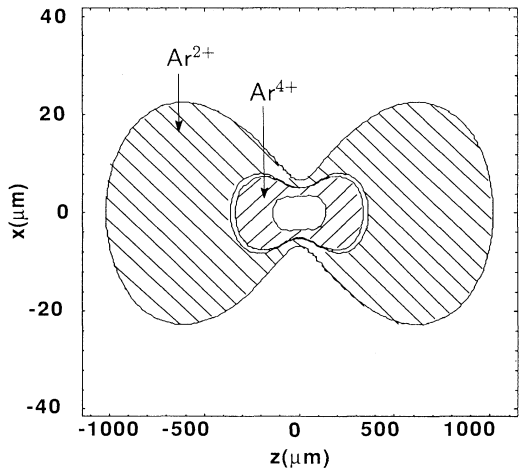

FIG. 4. The spatial distributions for Ar^{2+} and Ar^{4+} produced in a Gaussian beam with peak intensity of 10^{17} W/cm^2. The focus is for an f number of 5. The ions fall within borders defined by the threshold and saturation isointensity contours.

highest and the lower charge states further from the focus where the electric fields are lower. The small temporal overlap of the probabilities for a fixed intensity is apparent in the low spatial overlap of nonconsecutive charge states such as Ar^{2+} and Ar^{4+} at the end of the pulse.

For a Gaussian beam of peak intensity I_0, the volume [9] inside an isointensity boundary defined by I is

$$V=V_0[\tfrac{2}{9}\xi^3+\tfrac{4}{3}\xi-\tfrac{4}{3}\arctan(\xi)] , \tag{13}$$

where

$$\xi=\left[\frac{I_0}{I}-1\right]^{1/2} , \quad V_0=\frac{\pi^2 w_0^4}{\lambda} . \tag{14}$$

Equation (13) is the change of variable needed for the spatial integral. We can find the ion yield N_{k+1} for ion $k+1$ as a function of the peak intensity from

$$N_{k+1}=\rho\int_0^{I_0}\frac{dV}{dI}p_{k+1}dI , \tag{15}$$

where ρ is the density of the target gas.

A. Low-intensity limit of Eq. (15) and appearance intensities

The ion-yield curve for laser fields below the theoretical threshold fields calculated from Eq. (10) can be obtained in closed form by substituting Eq. (9), the low-intensity-field form of p_{k+1}, into Eq. (15) and performing the integration [19],

$$N_{k+1}=(6\omega_0 E_k)\left[\frac{2\tau}{1.76}\right]\rho(\pi V_0)(F_k+F_k^2+F_k^3) \times\exp\left[-\frac{1}{F_k}\right] , \tag{16}$$

where

$$F_k=\frac{F_0}{\frac{2}{3}E_k^{3/2}} . \tag{17}$$

Figure 5 compares Eq. (16) with the numerically integrated results. The two curves are numerically identical for intensities below the theoretical threshold intensity and diverge for intensities above it.

The experimental appearance field can be derived from Eq. (16) by finding the field at which N_{k+1} is equal to a few. For example the appearance field for $N_{\rm ap}$ ions is

$$F_{k+1}^{\rm ap}=\frac{\frac{2}{3}E_k^{3/2}}{\ln\left[\dfrac{(6\omega_0 E_k)(2\tau/1.76)\rho(\pi V_0)}{N_{\rm ap}}\right]} . \tag{18}$$

With $N_{\rm ap}$ set equal to 1, Fig. 6 shows the appearance intensity calculated from Eq. (18) plotted as a function of the ionization potential for three gas densities. This plot illustrates the density dependence of the appearance intensities in Eq. (18). Since density is a macroscopic property of the gas, we cannot associate an atomic interpretation to the appearance intensity.

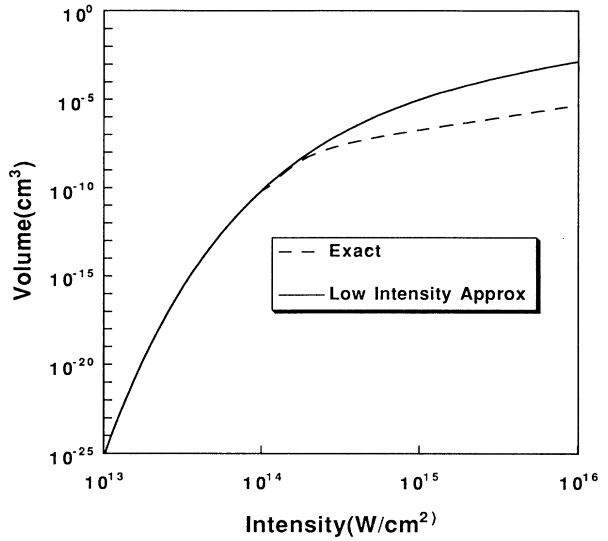

FIG. 5. The low-intensity limit, Eq. (16), of N_1/ρ, the density-normalized ion yield for Ar^{1+}, is compared to the numerically calculated results. The two curves diverge at the theoretical threshold intensity of Eq. (10), whose value in Table IV is 1.00×10^{14} W/cm^2.

The appearance intensity is relatively insensitive to all the parameters that are in the logarithmic denominator of Eq. (18). If we want to determine laser intensities from ion yields, then the appearance yield is a good measure of intensity because of this insensitivity. On the other hand, this insensitivity hinders our ability to distinguish atomic ionization models based on appearance intensities.

The important physics in Eq. (18) is that the appearance field strength is predominantly a $\frac{3}{2}$ power law with respect to the ionization potential and departs from this

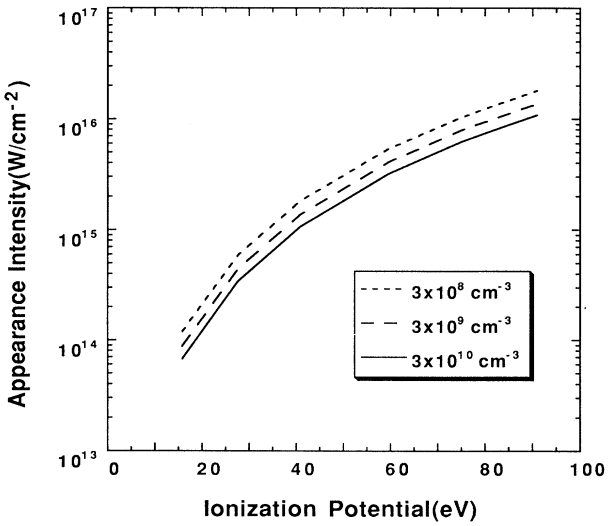

FIG. 6. The appearance intensity as a function of ionization potential is plotted for the three target gas densities of 3×10^8, 3×10^9, and 3×10^{10} cm^{-3}.

power law by the weak logarithmic denominator. The logarithmic term decreases the growth rate of the appearance field strength as the ionization potential increases. Furthermore the $\frac{3}{2}$ power law is common to the models in Tables I–III, while only the four models in Tables I and II possess the $\ln(E_k)$ factor in their denominators. On the other hand, the MPI model has in its denominator the factor of $E_k^{1/(2n)}$, where n is the number of photons needed for ionization, which is an upper bound [20] of $\ln(E_k)$. The $\frac{3}{2}$ power law arises from the $\frac{2}{3}E_k^{3/2}$ term for normalizing the laser field strength in the rate laws. This terms represents the intra-atomic forces acting on the electron to be removed by the laser and is the scale by which the laser field is measured [5]. On the other hand, the E_k in the $\ln(E_k)$ term of Eq. (18) arises from the numerical frequency factor $(6\omega_0 E_k)$ in the front of the rate law. This is the frequency of the electron's motion and the normalization of the time scale [5].

B. High-intensity limit of Eq. (15) and saturation intensities

The ion-yield curve for laser intensities above the saturation intensity in Eq. (12) can be obtained in closed form by substituting in Eq. (15) the asymptotic form of the volume Jacobian,

$$\frac{dV}{dI} \approx \frac{V_0}{3}\frac{I_0^{3/2}}{I^{5/2}} . \tag{19}$$

The integration domain in Eq. (15) is effectively I_{thres} to I_{sat} because p_{k+1} is vanishingly small for intensities beyond this range (see Fig. 2). Within this range p_{k+1} can be approximated by the unit function giving the ion yield as

$$N_{k+1}=\tfrac{2}{3}\rho(\tfrac{2}{9}V_0)\left[\frac{1}{(I_{k+1}^{\text{thres}})^{3/2}}-\frac{1}{(I_{k+1}^{\text{sat}})^{3/2}}\right]I_0^{3/2} . \tag{20}$$

The $\frac{2}{3}$ factor in Eq. (20) arises as follows. If we had approximated p_{k+1} by a parabola instead of the rectangular function, we would have obtained a more accurate approximation than Eq. (20). The result is slightly lower but more complicated than Eq. (20). The numerical factor is approximately equal to $\frac{2}{3}$, which is the ratio of the area of a parabola inscribed by a rectangular function to the area of the rectangular function.

Figure 7 compares Eq. (20) for k equal to one with the numerically integrated results. We find that the numerically integrated result approaches its asymptote, Eq. (20), at the saturation intensity given by Eq. (12) (the value from Table IV is 1.32×10^{15} W/cm^2). The ion-yield curve converges to its asymptotic limit at the saturation intensity because it is where the integral of Eq. (15) slows down to a $\frac{3}{2}$ power rate of growth with peak intensities. When I_0 increases from zero to I_{sat}, the integral in Eq. (15) increases for two reasons: (i) the range of integration increases, and (ii) the integrand is an increasing function of I_0. However, as I_0 goes beyond I_{sat}, p_{k+1} truncates the integrand. We accomplish the truncation by setting the upper limit of integration equal to I_{sat}. The truncation cuts off an avenue of growth for the integral, and thus reduces the integral's growth rate to a $\frac{3}{2}$ power law. This asymptotic dependence is commonly known as the "volume expansion effect [9]."

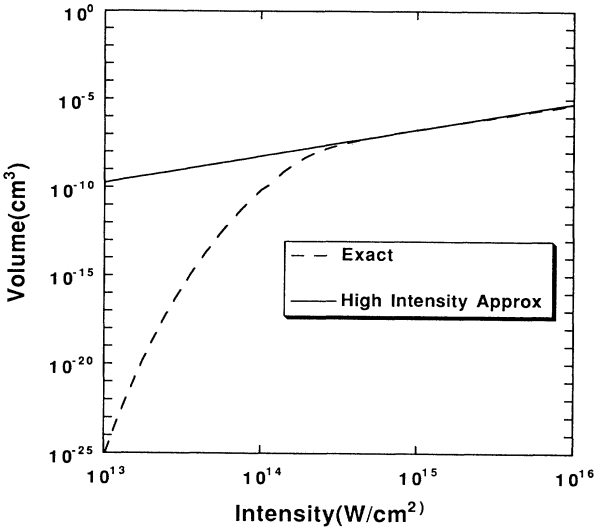

FIG. 7. The high-intensity limit, Eq. (20), of N_1/ρ, the density normalized ion yield, for Ar^{1+}, is compared to the numerically calculated result. The two curves converge at the saturation intensity of Eq. (12), whose value in Table IV is 1.32×10^{15} W/cm^2.

IV. INTEGRATING THE OTHER RATE LAWS

Let us demonstrate our integration method for the static case of a complex atom. The static complex atom rate can be written as

$$\Gamma_{\text{CA}}=\gamma_{\text{CA}}\left[\frac{1}{F_k}\right]^{P+1}\exp\left[-\frac{1}{F_k}\right] , \tag{21}$$

where F_k is the field strength divided by $(\frac{2}{3})E_k^{3/2}$, and F_k is the same normalized field strength given in Eq. (17). We define $P=2n-|m|-2$, where n, l, and m, are the standard quantum numbers of the electron's valence shell. Let us cast Eq. (21) into the form of the simple atom rate law by rewriting it as

$$\Gamma_{\text{CA}}=\gamma_{\text{CA}}\left[-\frac{\partial}{\partial\beta}\right]^{P}\frac{1}{F_k}\exp\left[-\frac{\beta}{F_k}\right] , \tag{22}$$

where β is a dummy variable we set equal to one at the end of the calculation, and γ_{CA} is a field independent coefficient.

By interchanging the order of integration and differentiation, we may write the total time integral of Eq. (22) as

$$\phi_{\mathrm{CA}}=\gamma_{\mathrm{CA}}\int_{-\infty}^{+\infty}dt\left[-\frac{\partial}{\partial\beta}\right]^{P}\frac{1}{F_k}\exp\left[-\frac{\beta}{F_k}\right], \tag{23a}$$

$$=\gamma_{\mathrm{CA}}\left[-\frac{\partial}{\partial\beta}\right]^{P}\int_{-\infty}^{+\infty}dt\frac{1}{F_k}\exp\left[-\frac{\beta}{F_k}\right]. \tag{23b}$$

Furthermore Eq. (23b) can also be expressed as

$$\phi_{\mathrm{CA}}=\gamma_{\mathrm{CA}}\left[-\frac{\partial}{\partial\beta}\right]^{P}\frac{1}{\beta}\int_{-\infty}^{+\infty}dt\frac{\beta}{F_k}\exp\left[-\frac{\beta}{F_k}\right]. \tag{24}$$

A comparison of Eqs. (8) and (24) shows that Eq. (24) can be expressed in closed form as

$$\phi_{\mathrm{CA}}=\gamma_{\mathrm{CA}}\left[\frac{2\tau}{1.76}\right]\left[-\frac{\partial}{\partial\beta}\right]^{P}\frac{1}{\beta}\left[\frac{\beta}{F_k}K_1\left[\frac{\beta}{F_k}\right]\right], \tag{25}$$

with the provision that β be set equal to 1 in Eq. (25) after the differentiation process.

We may also use this method to find the low-intensity form of the ion-yield curve, which is the volume integral of Eq. (25). Furthermore cycle averaging is the process of integrating over the phase of the E field. We note that differentiation by β commutes with both volume integration and phase integration. Therefore the other formulas in Tables I–III can be derived explicitly by this integration method.

V. THE SPECIES DEPENDENCE OF THE APPEARANCE INTENSITY

For the convenience of the reader, we reproduce here from Table II the appearance intensity for the complex-atom model [5,6],

$$F_{k+1}^{\mathrm{ap}}=\frac{\frac{2}{3}E_k^{3/2}}{\ln\left[\dfrac{\gamma_{\mathrm{CA}}(2\tau/1.76)\rho(\pi V_0)}{N_{\mathrm{ap}}}\right]}. \tag{26}$$

For the complex-atom model, Eq. (26) depends on the quantum numbers of the valence shell from which the electron escapes through the factor,

$$\gamma_{\mathrm{CA}}=\omega_0\frac{E_k}{2}G_{lm}\tilde{C}_{nl}^2, \tag{27}$$

which is the frequency scale of the complex-atom rate law. For completeness, the G_{lm} and $\tilde{C}^2$ terms in Eq. (27) are

$$G_{lm}=\frac{(2l+1)(l+|m|)!}{2^{|m|}(|m|)!(l-|m|)!}\frac{1}{3^{|m|}}, \tag{28}$$

and

$$\tilde{C}_{nl}^2=\left[\frac{2e^1}{n}\right]^{2n}\frac{1}{(2\pi n)}3^{2n-1}. \tag{29}$$

Figure 8 plots the appearance intensity calculated from Eq. (26) as a function of the ionization potential for different values of n corresponding to the valence shells of noble atoms He–Xe. We computed these curves with

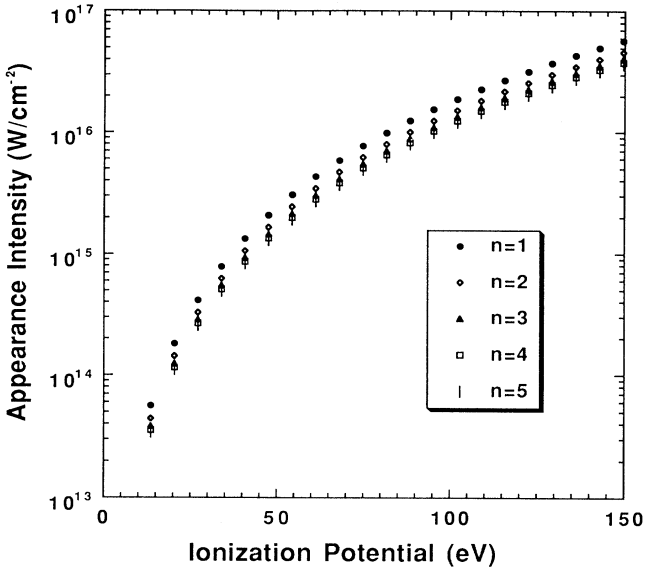

FIG. 8. The appearance intensity of the static complex-atom model for $n=1$, 2, 3, 4, and 5. These curves represent the appearance intensities of He, Ne, Ar, Kr, and Xe. The curves of lower n values lie above those of higher n values, which is ordering observed in the data of Augst and Gibson. The agreement can be improved by allowing for noninteger values of n (quantum-defect theory [21]), and by employing nonzero l and m values for the subshell dependence of Eq. (28).

l and m set equal to zero. The appearance intensities shown in Fig. 8 separate into a group of curves labeled by the principle quantum number n. The curves of smaller n values lie above those of larger n values. This ordering means that laser fields remove electrons from higher valence shells more easily than from lower valence shells (for a fixed ionization potential). This characteristic ordering was observed in the data of Augst (Fig. 2 of Ref. [17]) and of Gibson (Fig. 1(a) of Ref. [8]). We interpret the observed species dependence to be the principal-quantum-number dependence as suggested in Eq. (26). Substitution of the ionic charge Z and effective principle quantum number n^* for the ionization potential yields the same Z^6 dependence as derived in the barrier suppression model [7].

The appearance intensity decreases with increasing n because the γ term in the denominator of Eq. (26) is an increasing function of n (in the range of $1<n<5$). Our effective quantum-number dependence of this intensity is slightly stronger than $(n^*)^{-6}$. For comparison we point out that the barrier-suppression model predicts a $(n^*)^{-8}$ dependence. In Fig. 9, we plot $\tilde{C}^2$ as a function of n, and we can see that $\tilde{C}^2$ is a strongly peaked function of n. The appearance intensity is sensitive to n because $\tilde{C}^2$ is large enough to overcome the weakening effect that the logarithmic function has on it in Eq. (26). Furthermore Fig. 9 shows that $\tilde{C}^2$ peaks for a value of n close to 5.6. Consequently, Eq. (29) implies that for $l=m=0$ radon, which has a valence shell of $n=6$, should have the same or a higher appearance intensity than xenon. On the oth-

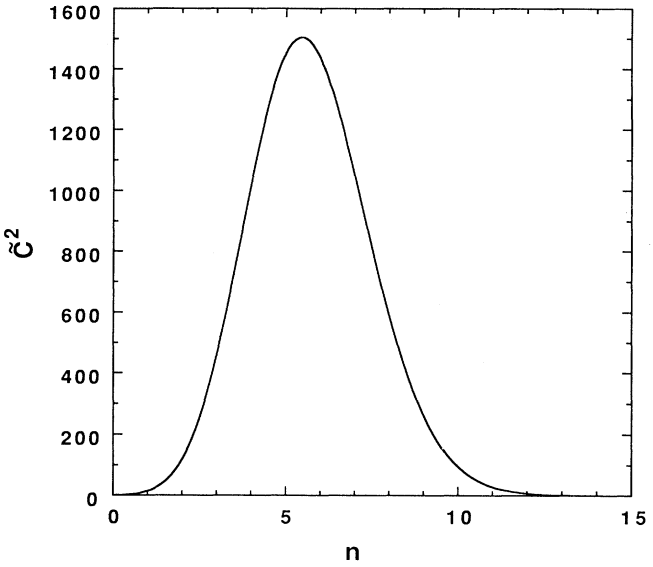

FIG. 9. The $\tilde{C}^2$ term as a function of n. For a free atom, $\tilde{C}^2$ decreases monotonically with n from the value of the order of 4. However, the external field makes $\tilde{C}^2$ nonmonotonic, and raises the peak value of $\tilde{C}^2$ to the order of 1500.

er hand, a simple extrapolation of the observed trend in the measured data would indicate otherwise.

We can understand the physics in the n scaling of the appearance intensity by recognizing that the $\tilde{C}^2$ factor comes from the normalization constant of a free-atom wave function, as well as the field strength of the laser. The normalization constant of a Coulomb wave function is a monotonically decreasing function of n. This decrease in $\tilde{C}^2$ induces an ordering that would be opposite to the observed ordering. However, the laser field changes the wave function into an autoionizing state. This change appears in the wave function through the normalization constant (Ammosov, Delone, and Krainov [6]). The laser causes $\tilde{C}^2$ to lose its monotonicity and to become a large peaked function of n.

There are two ways to improve the agreement between Eq. (26) and the measured data. The first is to use the Ammosov-Delone-Krainov [6] prescription of replacing n with n^* in Eq. (29) to account for quantum defects [21]. The agreement between theory and data can be improved further by using the appropriate quantum numbers of the subshell from which the electron is removed in Eq. (28). There is some ambiguity in the choice of l and m in the G_{lm} term of Eq. (28) because an ion has many configurations for a given valence. However, averaging over configurations should give judicious choices for l and m.

VI. CONCLUSION

The closed-form solution to the rate equations for the sequential case enables us to extend our understanding of strong-field ionization of gases by providing scaling laws for (i) threshold intensities, (ii) appearance intensities, (iii) saturation intensities, and (iv) the integrated ion yields as functions of laser intensities. These scaling laws also enable us to probe efficiently a large domain of atomic parameters. For example, we can examine the source of the species dependence of the appearance intensities for the inert gases. We predict that the appearance intensity curve for radon would not lie below the appearance intensity curve of xenon, if the theory [6] of Ammosov, Delone, and Krainov is correct. Given the validity of the ionization rates, such closed-form solutions aid in determining deviations from sequential ionization.

ACKNOWLEDGMENTS

We thank Abraham Szöke for his many insights into this problem, and for his guidance throughout this work. We also thank the L Division management of Lawrence Livermore National Laboratory for their support. This work was performed under the auspices of the U.S. Department of Energy by the Lawrence Livermore National Laboratory under Contract No. W-7405-Eng-48.

APPENDIX A: ERROR ANALYSIS OF EQ. (7)

The rate equations in Eq. (1) conserve probability. Therefore a test of Eq. (7) is its ability to conserve probability. We write the sum of the expressions in Eq. (7) as

$$\sum_{i=0}^{n} p_i = 1 + \sum_{i=1}^{n-1} \frac{\phi_i}{\phi_{i-1}} p_i \ . \tag{A1}$$

The sum on the right-hand side of Eq. (A1) is a global error of Eq. (7). One term dominates the error because for a given intensity all the p_i's except for one are small (see Fig. 2). The p_i that is large refers to the charge state that can be created without being ionized by the laser operating at the given intensity. Let us call this charge state j. The second sum in Eq. (A1) is then

$$\sum_{i=1}^{n-1} \frac{\phi_i}{\phi_{i-1}} p_i < (n-1) \frac{\phi_j}{\phi_{j-1}} \ . \tag{A2}$$

At the intensity where p_j is large, it is appropriate to use the asymptotic forms of ϕ_j and ϕ_{j-1} in Eq. (A2),

$$\sum_{i=1}^{n-1} \frac{\phi_i}{\phi_{i-1}} p_i < (n-1) \frac{E_j^{7/4}}{E_{j-1}^{7/4}} \exp\left[-\frac{2}{3F} (E_j^{3/2} - E_{j-1}^{3/2}) \right] \ . \tag{A3}$$

Hence the error of Eq. (7) is like $\exp(-1/F)$, and there is favorable comparison with the numerically calculated results.

APPENDIX B: THE RANGE OF VALUES FOR p_k IN EQ. (7)

The values of p_k in Eq. (7) range between zero and one, which we prove by showing that p_k is positive and has maximum values of at most one. p_k is positive because $[\exp(-\phi_{k-1}) - \exp(\phi_k)]/[\phi_k - \phi_{k-1}]$ is always positive. The maximum value of any p_k can be found easily from

its maximum with respect to τ. Let H_k be the factor that multiplies τ in Eq. (8), then Eq. (7) can be expressed simply as

$$p_k = H_{k-1} \frac{\exp(-H_{k-1}\tau) - \exp(-H_k\tau)}{H_k - H_{k-1}} . \quad \text{(B1)}$$

Solving for $dp_k/d\tau = 0$, we find the maximum value of p_k to be

$$p_k = \alpha^{\alpha/(1-\alpha)} , \quad \text{(B2)}$$

where

$$\alpha = \frac{H_k}{H_{k-1}} . \quad \text{(B3)}$$

Therefore p_k is less than or equal to 1 for all positive values of α.

[1] N. H. Burnett and G. D. Enright, IEEE J. Quantum Electron. **26**, 1797 (1990).

[2] C. J. Joshi *et al.*, IEEE Trans. Plasma Sci. **18**, 814 (1990).

[3] A. McPherson *et al.*, J. Opt. Soc. Am. B **4**, 595 (1987).

[4] M. Ferray *et al.*, J. Phys. B **21**, L31 (1988).

[5] A. M. Perelomov, V. S. Popov, and M. V. Terent'ev, Zh. Eksp. Teor. Fiz. **50**, 1393 (1966) [Sov. Phys. JETP **23**, 924 (1966)].

[6] M. V. Ammosov, N. B. Delone, and V. P. Krainov, Zh. Eksp. Teor. Fiz. **91**, 2008 (1986) [Sov. Phys. JETP **64**, 1191 (1986)].

[7] S. Augst, D. Strickland, D. D. Meyerhofer, S. L. Chin, and J. H. Eberly, Phys. Rev. Lett. **63**, 2212 (1989).

[8] G. Gibson, T. S. Luk, and C. K. Rhodes, Phys. Rev. A **41**, 5049 (1990).

[9] M. D. Perry, O. L. Landen, A. Szöke, and E. M. Campbell, Phys. Rev. A **37**, 747 (1988).

[10] The integrated ion-yield ratio curves as functions of peak laser intensity may also serve as continuous diagnostics of peak laser intensity because these curves are rigorously independent of pressure.

[11] L. D. Landau and E. M. Lifshitz, *Quantum Mechanics Non-Relativistic Theory,* 2nd ed. (Pergamon, Oxford, 1965), Sec. 77.

[12] P. Lambropoulos, Phys. Rev. Lett. **55**, 2141 (1985).

[13] We have also derived closed-form solutions to the rate equations that include multiple ionization (nonsequential) to assess the validity of the sequential ionization assumption.

[14] A. L'Huillier, L. A. Lompré, G. Mainfray, and C. Manus, J. Phys. B **16**, 1363 (1983).

[15] D. N. Fittinghoff, P. R. Bolton, B. Chang, and K. C. Kulander, Phys. Rev. Lett. **69**, 2642 (1992).

[16] B. W. Boreham and J. L. Hughes, Zh. Eksp. Teor. Fiz. **80**, 496 (1981) [Sov. Phys. JETP **53**, 252 (1981)].

[17] F. Yergeau, S. L. Chin, and P. Lavigne, J. Phys. B **20**, 723 (1987).

[18] *Handbook of Mathematical Functions,* 10th ed., edited by M. Abramowitz and I. A. Stegun (U.S. Dept. of Commerce, Washington, DC, 1972), p. 1046.

[19] I. S. Gradshteyn and I. M. Ryzhik, *Table of Integrals, Series, and Products,* corrected and enlarged edition (Academic, New York, 1980), p. 1160. The key integrals can be found in Eq. (6.596.3).

[20] *Handbook of Mathematical Functions* (Ref. [18]), Eq. (4.1.37).

[21] M. J. Seaton, Rep. Prog. Phys. **46**, 167 (1983).